

The estimation of permeability of a porous medium with a generalized pore structure by geometry identification

S. M. Rezaei Niya and A. P. S. Selvadurai

Citation: *Physics of Fluids* **29**, 037101 (2017); doi: 10.1063/1.4977444

View online: <http://dx.doi.org/10.1063/1.4977444>

View Table of Contents: <http://aip.scitation.org/toc/phf/29/3>

Published by the *American Institute of Physics*

Articles you may be interested in

[On predicting receptivity to surface roughness in a compressible infinite swept wing boundary layer](#)

Physics of Fluids **29**, 034102034102 (2017); 10.1063/1.4977092

[Nonlinear simulation and linear stability analysis of viscous fingering instability of viscoelastic liquids](#)

Physics of Fluids **29**, 033101033101 (2017); 10.1063/1.4977443

[Modulating flow and aerodynamic characteristics of a square cylinder in crossflow using a rear jet injection](#)

Physics of Fluids **29**, 015103015103 (2017); 10.1063/1.4972982

Searching?
**Trust
CiSE.**

Google Scholar search results for "python in scientific computing". The top result is "Python for scientific computing" by TE Oliphant, published in *Computing in Science & Engineering*, 2007. The snippet reads: "By itself, Python is an excellent scripting language for scientific computing. However, with additional basic tools, Python transforms it into a language suited for scientific and engineering code that's often faster than C. Cited by 690. Related articles. All 12 versions. Cite. Save."

Book cover: *Computing in Science & Engineering* by TE Oliphant, published by NERSC.

It's peer-reviewed and appears in the IEEE Xplore and AIP library packages.

The estimation of permeability of a porous medium with a generalized pore structure by geometry identification

S. M. Rezaei Niya and A. P. S. Selvadurai

Department of Civil Engineering and Applied Mechanics, McGill University, 817 Sherbrooke Street West, Montreal, Quebec H3A 0C3, Canada

(Received 24 October 2016; accepted 10 February 2017; published online 3 March 2017)

The paper presents an approach for estimating the permeability of a porous medium that is based on the characteristics of the porous structure. The pressure drop in different fluid flow passages is estimated and these are combined to evaluate the overall reduction. The theory employed is presented and the level of accuracy for different cases is discussed. The successive steps in the solution algorithm are described. The accuracy and computational efficiency of the approach are compared with results obtained from a finite-element-based multiphysics formulation. It is shown that for a comparable accuracy, the computational efficiency of the approach can be two orders of magnitude faster. Finally, the model predictions are examined with conventional relationships that have been reported in the literature and are based on permeability-porosity relationships. It is shown that estimating the permeability of a porous medium using porosity can lead to an order of magnitude error and the expected permeability range in different porosities is presented using 10 000 random structures. *Published by AIP Publishing.* [<http://dx.doi.org/10.1063/1.4977444>]

I. INTRODUCTION

The property of permeability of a porous medium has applications in a variety of areas in engineering and materials science. Although it is not clear at first sight, the fundamental topic of research in the various fields is the examination of flow and transport in porous media. Because of the complexity of the subject, the experimental approach is the most common method used to study how the porous structure affects the mass transport. In essence, the required parameter (e.g., diffusivity or permeability) is measured for different porous media and an experimental relationship is established, representing an “effective” coefficient (e.g., effective diffusivity).¹ Based on experimental studies, theoretical relations (e.g., the Carman-Kozeny equation or the Bruggeman’s relation²) have been developed to obtain better representations for estimating transport parameters.

Despite the general success of experimental approaches, the following points have been raised concerning the applicability of these methods to generalize the results for a quantitative estimation of permeability of porous media:

- The complexity of the measuring procedure can influence the precision of the results to the level that the variations of measured permeability because of the changes in the input parameter (e.g., porosity) cannot be easily distinguished from the uncertainties in the measurements (e.g., Ref. 3).
- Porosity is often the only “characteristic” parameter that is used to describe the porous medium. However, different porous structures with the same porosity can exhibit wide variation in the transport pattern⁴ (also see Figure 1). Although the schematics

presented in Figure 1 show extreme cases, similar pore structure distributions have been discussed in the past.⁵

- Several attempts have been made to define other characteristic parameters for porous structures^{6,7} of which tortuosity is the most common. However, tortuosity is not measured directly and is considered as a correlation factor or is estimated simply from the porosity value.⁸
- The generalization of the measured trends is questionable. The dominant characteristic parameter of a porous medium that governs flow is not clear and therefore the measured trends cannot be generalized to “similar” porous media because the similarity is imprecisely interpreted. Specifically, permeability values are normally non-dimensionalized using the solid phase particle diameter; however, it is reasonable to expect, at least in natural porous structures, that there will be a range of particle sizes.

When the above challenges associated with the experimental characterization of porous materials are considered, the development of numerical models to capture the porous structure and transport mechanisms merits attention. There have been many numerical modeling approaches developed to simulate transport in porous media (especially in random structures^{9–12}) and a comprehensive review of different strategies is presented in Ref. 13. The review covers continuum-scale approaches where the high computational resources required resulted in imposing restricted or unrealistic assumptions. It also covers the pore-scale modeling approaches, which are essentially more powerful for modeling specific physical phenomena (such as viscous fingering). However, in spite of their strength, those models are generally

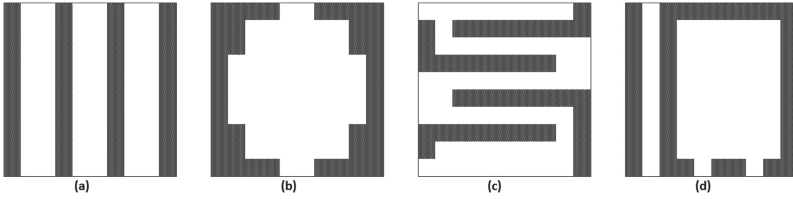


FIG. 1. Four different pore structures with the same porosity (60%).

restricted by limited access to computational resources (specifically the Lattice-Boltzmann method).¹³ The most common pore-scale approach, which needs considerably less computational time and resources, is pore-network modeling. This method has frequently been used to study multiphase transport in porous media [e.g., Refs. 14–16]; however, it too has shortcomings¹³ in that the geometries employed are often far from the physical reality of a pore structure and concepts such as “pore” and “throat” are subjective and not always physically meaningful (e.g., mesh-based porous media). This issue is clearly evident in the examples (a) and (c) shown in Figure 1.

The scope of the present research is to develop a new modeling approach for mass transport in porous structures that can capture the geometrical details of a porous medium. This approach requires considerably less computational resources than computational fluid dynamics approaches and allows researchers to study and optimize the details of the porous structures (specifically, during the design and optimization phases for engineered porous materials). For this reason, the modeling approach needs to be based on analytical estimates that provide acceptable accuracy. Here, a new model for estimating the viscous pressure drop in an arbitrary porous structure is presented as the first step towards accomplishing an analytical-based modeling approach.

In this paper, the theoretical analysis required for the modeling is discussed first. Next, the modeling approach is explained and the details at each step are presented and discussed. The model predictions are then verified against the modeling results obtained using both the COMSOL™ Multiphysics computational fluid dynamics (CFD) package and the measured permeability values from estimates reported in the literature. Finally, the permeability-porosity relationship is examined and discussed as an example of the model applications. It is shown that the permeability estimates obtained using the porosity value for an unknown structure can easily result in errors of several orders of magnitude.

II. THEORY

In this section we discuss the slow viscous flow model in 2D and show that the pressure drop across any flow passage can be estimated to within an accuracy of 10% by estimating the average length of the streamline based on the length of the surrounding boundaries. This estimate is used in Sec. III to determine the pressure drop across any arbitrary porous structure. In this section, the analytical approach and the accuracy for different classical examples are presented. In particular, the pressure losses in parallel channels, stagnation-

point flow, arbitrary joints, and step flow are estimated. In all cases, the flow regime at the entrance and the exit is assumed to be fully developed (purely axial with variations only in the lateral coordinates).

A. Parallel channel

Fluid flow in a parallel channel has been solved analytically and this is known as the parallel plate assumption.¹⁷ In this type of flow, the pressure gradient dp/dx can be easily determined from the flow rate per unit thickness normal to the flow plane (Q) using the following equation:¹⁷

$$Q = \frac{h^3}{12\mu} \left(-\frac{dp}{dx} \right), \quad (1)$$

where h and μ are the width of the channel and the dynamic viscosity of the fluid, respectively. Equation (1) shows that for a constant flow rate, the pressure drop is a linear function of the channel length (dp/dx is constant), clarifying that this method (estimating the pressure drop from the length of the surrounding boundaries) gives an accurate analytical prediction in the parallel channel case.

B. Stagnation-point flow

In order to discuss the analytical estimates employed in Sec. III, we consider the pressure drop on a streamline in a creeping flow. Employing the Stokes equation¹⁷ in streamline coordinates for the steady flow (see Appendix A), the pressure drop rate along the streamline can be calculated if the Laplacian of the velocity can be obtained (Eq. (A4)). The stagnation-point flow is discussed here in order to explain the details of the process. To our knowledge, there is no analytical solution for the viscous flow problem at a corner region. In our approach, the problem is modified to that shown in Figure 2.

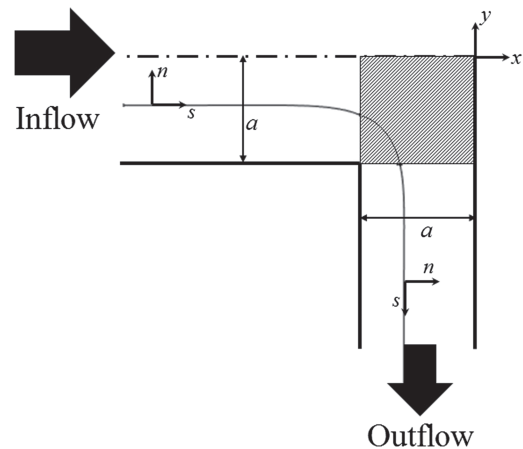


FIG. 2. The schematic of the stagnation-point flow.

The flow is bounded by two parallel boundaries at the outflow, while the inflow region is defined by a surrounding boundary and the plane of symmetry ($y = 0$).

The flow is considered fully developed at the inflow and the outflow; as a result, the flow rates and the Laplacian of the velocity vector (\mathbf{V}) can be determined. Considering the inflow width ($2a$), it can be shown that at the inflow region,

$$Q = \frac{a^3}{3\mu} \left(-\frac{dp}{dx} \right), \quad (2)$$

$$|\nabla^2 \mathbf{V}| = \frac{\partial^2 u}{\partial x^2} + \frac{\partial^2 u}{\partial y^2} = -\frac{3Q}{a^3}. \quad (3)$$

Here, u and v are the velocity components in the x and y directions, respectively. We note that the flow rate (Q) in Equation (2) is half of the total inflow flow rate and is in fact the flow rate entering the geometry shown in Figure 2.

Similarly, it can be shown that at the outflow region,

$$Q = \frac{a^3}{12\mu} \left(-\frac{dp}{dy} \right), \quad (4)$$

$$|\nabla^2 \mathbf{V}| = \frac{\partial^2 v}{\partial x^2} + \frac{\partial^2 v}{\partial y^2} = -\frac{12Q}{a^3}. \quad (5)$$

As can be seen in Figure 2, the streamline coordinates s and n in the downstream region are parallel to the y and x axes, respectively. Equations (3) and (5) show that the Laplacian of the velocity vector is equal to $-\frac{3Q}{a^3}$ upstream and $-\frac{12Q}{a^3}$ downstream. To estimate the pressure drop along the streamline, the following assumptions are employed:

1. The flow remains fully developed for all the regions outside the shaded area in Figure 2. In other words, the velocity distributions follow the fully developed assumption for $x < -a$ and also $y < -a$. This assumption is revisited in the next paragraphs.
2. The average of the Laplacian changes linearly from the upstream value ($-\frac{3Q}{a^3}$) to the downstream value ($-\frac{12Q}{a^3}$) in the shaded area.

Using these assumptions, the pressure gradient in the shaded area can be estimated as

$$\frac{\partial p}{\partial s} = \mu \left(-\frac{3Q}{a^3} - \frac{9Q}{a^3} \frac{s}{S_t} \right), \quad (6)$$

where s is the streamline coordinate in the shaded area and S_t is the total average length of the streamlines in the shaded area (referring to Figure 2, (s) = 0 at the beginning of the shaded area and $s = S_t$ at the end of shaded area). As a result, the overall pressure drop in the shaded area can be determined by integrating the above equation as

$$\Delta p = -\frac{3\mu Q}{a^3} S_t - \frac{9\mu Q}{a^3} \frac{S_t}{2}. \quad (7)$$

The streamline length, however, can vary from asymptotically zero close to the rotation corner ($-a, -a$) to $\sim 2a$ for the longest streamline, which enters the shaded area close to the symmetry line and exits the shaded area close to the boundary $x = 0$. As a result, the average length of the streamlines in the shaded area can be estimated to be close to a . Using this assumption, the

pressure drop of the flow in the shaded area in Figure 2 can be estimated as

$$\Delta p_{avg, \text{ Hatched Area}} = -\frac{15\mu Q}{2a^2}. \quad (8)$$

A comparison of the pressure loss predictions from the above approximation procedure and the modeling of this stagnation point flow in COMSOL™ Multiphysics software using Stokes flow assumption shows that the overall error of this approximation procedure is less than 1.5%. This shows that estimating the pressure drop using the average length of the surrounding boundaries gives a result of reasonable accuracy.

It should be mentioned that the assumption of a fully developed velocity distribution outside the shaded area is not expected to introduce significant error. While the velocity distribution can be distorted before and after the shaded area by the stagnation point effects, these distortions nullify their impacts on the estimations presented above. In other words, while the Laplacian term can be smaller than $-3Q/a^3$ before the shaded area, the assumption of a fully developed velocity distribution upstream of the shaded area overestimates the pressure drop before the shaded area (by assuming that the Laplacian term remains at $-3Q/a^3$) and simultaneously under-estimates the pressure drop inside the shaded area (by assuming that the Laplacian term changes from the $-\frac{3Q}{a^3}$ value to the final value) and finally, the impact of these over- and under-estimations will be nullified.

C. Flow of an arbitrary joint

The pressure drop and the flow rate ratio in an arbitrary joint can also be estimated using the same approach. The schematic of an arbitrary joint is shown in Figure 3. The flow enters a channel of width a from the left with a flow rate of Q_a and exits from two channels of widths b and c with flow rates of Q_b and Q_c , respectively. This flow rate partitioning has to be estimated.

Similar to the stagnation-point flow, the velocity distributions outside the shaded area are assumed to be fully developed. As a result, the Laplacian of the velocity vector in the different channels can be estimated as

$$|\nabla^2 \mathbf{V}|_a = \frac{-12Q_a}{a^3}, \quad |\nabla^2 \mathbf{V}|_b = \frac{-12Q_b}{b^3}, \quad |\nabla^2 \mathbf{V}|_c = \frac{-12Q_c}{c^3}. \quad (9)$$

Using similar assumptions (e.g., the Laplacian changes linearly inside the shaded area), the pressure drop inside the shaded area from channel a to channels b and c can be estimated as before as

$$\Delta p_{ac} = -6\mu S_{ac} \left(\frac{Q_a}{a^3} + \frac{Q_c}{c^3} \right), \quad (10)$$

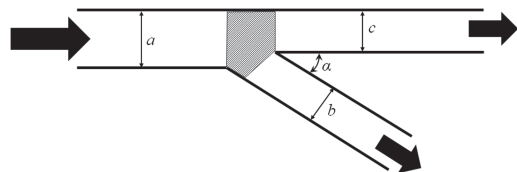


FIG. 3. The schematic of an arbitrary joint.

$$\Delta p_{ab} \approx -6\mu S_{ab} \left(\frac{Q_a}{a^3} + \frac{Q_b}{b^3} \right), \quad (11)$$

where S_{ac} and S_{ab} are the average lengths of the streamlines from channel a to channels c and b , respectively, which can be estimated by assuming that the average length of the streamlines in the shaded area in Figure 3 is an average of the length of the surrounding boundaries for each section of the flow as follows:

$$S_{ab} \approx \frac{1}{2} \left(\frac{b}{\tan \alpha} + S_{\max} \right), \quad (12)$$

$$S_{ac} \approx \frac{1}{2} \left(\frac{b}{\sin \alpha} + S_{\max} \right). \quad (13)$$

Here, S_{\max} is the length of the streamline that separates the flow rates. In other words, the streamlines above this specific streamline move to channel c , while the streamlines below move to channel b . The other terms in Equations (12) and (13) estimate the length of other surrounding boundaries for each flow (i.e., length of the upper side of the shaded area in Figure 3 for S_{ac} and length of the bottom left side of the shaded area for S_{ab}). S_{\max} can be estimated as

$$S_{\max} \approx \sqrt{t^2 + \left(\frac{b}{\sin \alpha} \right)^2}. \quad (14)$$

The parameter t in the above relationship refers to the distance from the lower boundary in channel a through which the flow rate of Q_b occurs. As an example, if Q_b becomes $0.5Q_a$, then t would be equal to $0.5a$. Considering the fully developed velocity profile assumption in channel a , this parameter can be determined from the following equation:

$$2 \left(\frac{t}{a} \right)^3 - 3 \left(\frac{t}{a} \right)^2 + \frac{Q_b}{Q_a} = 0. \quad (15)$$

To solve the above equation, the flow rate in channel b has to be determined. As the flow is assumed to be fully developed outside the shaded area, the pressure drop in channels b and c can be estimated using Equation (1) as a linear function of the flow rates,

$$\Delta p_b = \varphi_b Q_b, \quad \Delta p_c = \varphi_c Q_c, \quad (16)$$

where φ_b and φ_c are constants. Using the equal-exit-pressure assumption, the pressure drop from both paths b and c has to be equal,

$$\Delta p_{ab} + \Delta p_b = \Delta p_{ac} + \Delta p_c. \quad (17)$$

Using Eqs. (10), (11), and (16), and the principle of conservation of mass ($Q_c = Q_a - Q_b$), the flow rate in section b can be calculated as

$$\begin{aligned} & \left[\frac{S_{ab}}{b^3} + \frac{S_{ac}}{c^3} + \frac{\varphi_b + \varphi_c}{-6\mu} \right] Q_b \\ &= \left[\frac{S_{ac}}{a^3} + S_{ab} \left(\frac{1}{c^3} - \frac{1}{a^3} \right) + \frac{\varphi_c}{-6\mu} \right] Q_a. \end{aligned} \quad (18)$$

The pressure drops in the shaded area can then be determined from Eqs. (10) and (11). It is necessary to mention that because of the assumptions employed during the calculation of the

lengths of the streamlines, the pressure drops will not necessarily satisfy Eq. (17) and as a result, the S_{ac} parameter has to be corrected as follows:

$$S_{ac} = S_{ab} \frac{\frac{Q_a}{a^3} + \frac{Q_b}{b^3}}{\frac{Q_a}{a^3} + \frac{Q_c}{c^3}} + \frac{1}{6\mu} \frac{\varphi_c Q_c - \varphi_b Q_b}{\frac{Q_a}{a^3} + \frac{Q_c}{c^3}}. \quad (19)$$

Finally, the solution algorithm can be summarized as follows:

1. As a first estimate, t is assumed to be equal to $a/2$.
2. S_{\max} is then determined from Equation (14).
3. S_{ab} and S_{ac} are estimated using Equations (12) and (13), respectively.
4. Q_b is obtained from Equation (18). Q_c is determined from the result $Q_c = Q_a - Q_b$.
5. Equation (15) is used to update t .
6. The algorithm is repeated from step 2 until convergence is achieved. The only correction is that S_{ac} has to be determined from Equation (19) instead of Equation (13).
7. The pressure drops in the shaded area are calculated using Equations (10) and (11).

The pressure drops and the flow rates predicted by this estimation procedure are compared with the modeling results obtained from the Stokes flow for identical geometries using COMSOL™ Multiphysics. The results are shown in Table I; the errors for both pressure drop and flow rates are less than 5% in the cases studied, while the flow rate estimation is considerably more accurate.

D. Step flow

A similar approach is employed in this section to estimate the pressure drop for a step flow region. The pressure drop is calculated using the average length of

TABLE I. The errors observed from the theory for different cases.

Arbitrary joint						
Case number	b/a	c/a	α	Flow rate error (%)	Pressure drop error (%)	
1	0.5	1	45°	0.7	1.3	
2	0.5	1	30°	1.1	4.3	
3	1	1	90°	0.85	4	
Step						
Case number	b/a			Error (%)		
1	1.5			0.9		
2	2			3.5		
3	3			8.8		
Geometries shown in Figure 5						
Case	k/A			Elapsed time (s)		
	Model	COMSOL	Error (%)	Model	COMSOL	Ratio
a	2.06×10^{-3}	2.29×10^{-3}	10	0.042	5	119
b	2.75×10^{-3}	2.86×10^{-3}	3.8	0.043	6	139
c	1.61×10^{-3}	1.51×10^{-3}	6.6	0.055	6	109
d	1.75×10^{-4}	1.77×10^{-4}	1.1	0.033	6	181

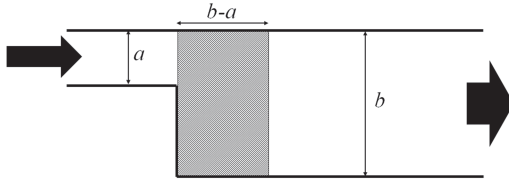


FIG. 4. The schematic of the geometry for a step flow.

the streamlines and linear-change-of-the-Laplacian-of-the-velocity-vector assumption. A schematic of a step flow is shown in Figure 4.

Here again, the flow is assumed to be fully developed outside the shaded area. The shaded area is considered to be the length over which the flow is adjusted to the new width. The length of this area is regarded as equal to the required width increment. The pressure drop in this area is estimated by assuming that the average length of the streamlines is equal to the average of the length of the boundaries surrounding the flow, i.e.,

$$S_{avg} = \frac{(b-a) + 2(b-a)}{2} = \frac{3(b-a)}{2}. \quad (20)$$

The pressure drop outside the shaded area is calculated using Equation (1). Inside the shaded area, however, the pressure drop is estimated by assuming that the Laplacian term changes linearly from its value in channel a ($-\frac{12Q}{a^3}$) to its value in channel b ($-\frac{12Q}{b^3}$). The overall pressure drop is then calculated and compared with the Stokes flow modeling for the same geometry, using the COMSOL™ Multiphysics software. The results are shown in Table I. As can be seen in the table, the errors are within an acceptable range. The largest error (8.8%) occurs when the flow passes through a step that is magnified three times ($b = 3a$). Even in this case, if the symmetry condition is enforced on the geometry and the input is moved to the center, the error drastically reduces to 0.15%.

Using the analysis and the procedure presented here indicates that the pressure drop of the Stokes flow in a passage can be evaluated by measuring the average length of the streamlines, which can be estimated from the average length of the surrounding boundaries of the passage. This observation is employed in Sec. III to estimate the pressure drop in any arbitrary two-dimensional porous structure. The flow rate distribution in different passages has to be determined such that the pressure drop of the parallel passages becomes equal. This process is discussed and explained in Sec. III.

III. SOLUTION ALGORITHM

The purpose of this section is to present the solution algorithm for estimating the pressure drop for any 2D porous structure. The solution procedure is explained in the subsections of Appendix B through an example. The pressure drop estimation is based on the analytical approximation presented previously; while this approximation is not as accurate as classical CFD methods (e.g., finite volume or finite difference), a calculation of the governing equations in each cell is not required, which decreases the computational demands drastically. In other words, the accuracy level is independent of the

mesh structure and size and is directly related to the accuracy of the analytical estimation employed in the process. Specifically, if a more accurate analytical approximation than the analysis presented in Sec. II is used, this algorithm can easily be adjusted and the accuracy improved without loss of generality.

In this method, the mesh is only required to capture the geometry of the porous structure. As a result, the mesh can be as coarse as the feature size of the structure. Here, a hexagonal mesh is used instead of the customarily employed rectangular mesh. The hexagonal mesh is preferred since the coverage of the neighborhood of a cell by adjacent cells is considerably higher than the coverage obtained using a rectangular mesh. In essence, in the rectangular mesh structure, the mass transport is normally considered from the east (E), west (W), north (N), and south (S) neighbor cells directly to the cell in each calculation step. As a result, there is no direct path for transport from the north-east (N-E), north-west (N-W), south-east (S-E), and south-west (S-W) cells to the cell. However, in the hexagonal mesh structure, each cell is surrounded by six adjacent cells, which are all directly accessible. Hence, the ratio of *disconnected* area around a cell (i.e., the ratio of the area of a circular space around a cell that belongs to those cells that are not directly connected to the cell) decreases from 30.9% in a 2D rectangular mesh to 14.7% in a 2D hexagonal mesh.

First, the passages for the fluid flow inside the porous structure are defined and the network of the structure is determined. When the passages are determined, the pressure drop in each passage can be estimated as a function of the flow rate using the analysis presented in Section II. Clearly, as the flow rates of the passages have not been estimated, the pressure drop value still needs to be determined. To find the flow rate distribution in the structure, a modified version of the Hardy Cross method is used, which is explained in Appendix B. To use this iterative method, it is necessary to have an initial estimate for the flow rate distribution which satisfies the continuity. For this reason, dead-end passages have to be excluded from the flow network of the structure.

As mentioned in Sec. II, the pressure drop in the connection region (shaded area in Figure 3) also needs to be estimated. For this calculation the flow rate has to be determined. However, a calculation of the flow rate distribution requires that the pressure drops have to be estimated first. While this issue can be solved using an iterative method, an initial estimate for the flow rates is made and the connection losses are determined accordingly. As the connection losses are expected to be considerably smaller than the pressure reduction within the passages, this assumption is not expected to affect the final results significantly.

IV. RESULTS AND DISCUSSIONS

In this section, the model predictions are compared with the modeling results for the same geometries obtained using the COMSOL™ Multiphysics CFD package and the measured permeability values reported in the literature.^{18–33} Initially, the pressure drop is calculated and then the permeability values are determined. The permeability is then

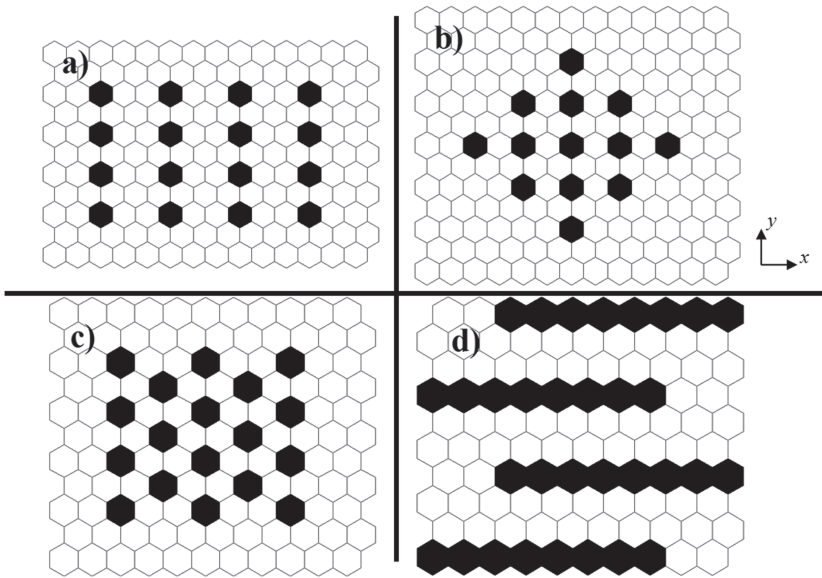


FIG. 5. Structure samples used for comparison in Table I with the porosities of (a) 90%, (b) 92%, (c) 85%, and (d) 68%.

non-dimensionalized using the total area of the region. In each case, it is assumed that the flow enters from the bottom and exits from top. The geometries and the particle arrangements of the samples are shown in Figure 5, while the results are shown in Table I. Table I also shows the ratio of the elapsed times for both methods on an i7-4510U laptop. The model predictions were obtained from an in-house coding of the algorithm using MATLAB™. Table I shows that while the error of the algorithm is less than 10% in all the cases studied, the elapsed computational time is two orders of magnitude faster. Figure 5(d) requires special attention as the overall flow direction in this sample is in the x direction. As can be seen in the table, the estimation error is in the same range for all the samples as the width estimation algorithm is not limited to the flow in the y direction.

Figure 6 compares the model predictions for squared arrays of solid cylinders in a transverse flow against the

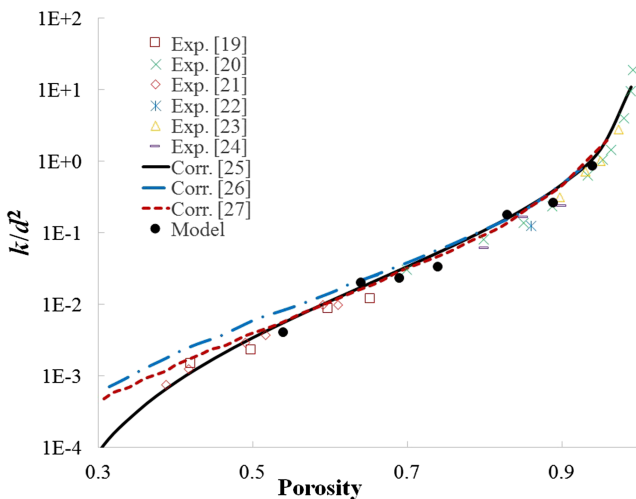


FIG. 6. The correlations and the measured values reported in the literature^{19–27} for the permeability of squared arrays of solid cylinders in transverse flow are compared against the model predictions.

measured non-dimensional permeability (k/d^2 , where d is the diameter of the solid units) and the reported correlations available in the literature.^{25–27} As shown in Figure 6, the permeability values predicted by the model are in agreement with the measured values. As the solid cylinders are arranged on a squared array in this figure, the deviation between the reported measured values is considerably limited compared to random structures such as those shown in Figure 7.

Figure 7 shows the measured permeability values and the predictions of permeability-porosity correlations reported in the literature for random 3D structures. As it can be seen in Figure 7, the reported measured permeability values for equal porosity values have up to one order of magnitude deviation in some cases. It should be noted that the measured values that are too far from the expected ranges are not normally reported [e.g., Ref. 18]. The figure also shows the predictions

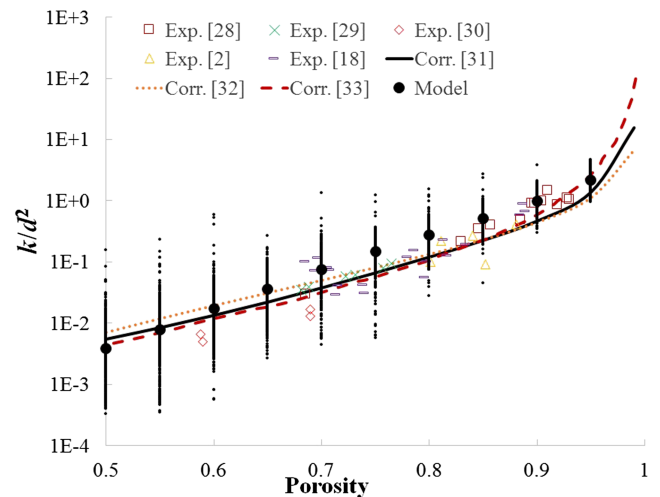


FIG. 7. The correlations and the measured values reported in the literature^{2,18,28–32} for the permeability values of different 3D structures are compared against the model predictions. The medians of the modeling results are shown in black solid circles, while each single modeling result is shown by a black dot.

of the model with different porosities. For each porosity value, 1000 completely random porous structures were developed and the permeability values for each structure were determined and recorded. The figure shows that the non-dimensional permeability can vary by two orders of magnitude for constant porosity values, which shows the unreliability of permeability-porosity correlations. Table II shows the mean, median and the 95%-confidence-interval range (in the logarithmic scale) of the permeability values for different porosities. It can be seen that the medians are consistently smaller than the mean values, showing that there are outliers with higher permeability values. Both Figure 7 and Table II show that the deviation is considerably higher for lower porosity values and decreases as the porosity increases. The results indicate that porosity is not a reliable measure of a random structure and any permeability correlation for an unknown structure based on porosity can easily result in an order of magnitude error. Nevertheless, the porosity values reported in Table II can be used for an unknown porous structure while the reported ranges have to be considered.

Finally, it is necessary to re-emphasize that the presented modeling approach is based on a 2D Stokes flow assumption. While the real 3D pore structures are normally far more complicated than the 2D approximations, the existing correlations for permeability estimation even for 2D pore structures or transverse flows in general cases are still not reliable, which highlights the need for new 2D approaches. Moreover, Figure 7 shows that the 2D model predictions are normally in the same range as 3D measurements, which shows that the 2D general studies can lead to a better understanding of the 3D fluid transport process. Also, the errors that occur using the Stokes flow approximation need to be considered for high flow rates and at high Reynolds numbers. Nevertheless, results such as those presented in Table II are still meaningful as they do not have 3D non-creeping flow counterparts. In brief, although this modeling approach is less accurate than other pore-scale modeling approaches (smoothed particle hydrodynamics, level-set, percolation, and Lattice-Boltzmann), the computational resources required are drastically less.¹³ In addition, whilst the mentioned methods can easily be applied to 3D problems, this model is specifically developed for 2D

TABLE II. The statistical parameters of the modeling results for k/d^2 in different porosities. The range column shows the 95% confidence interval of the values in the logarithmic scale.

Porosity	Permeability (k/d^2)		
	Mean	Median	Range
0.5	0.005 44	0.003 9	0.000 777-0.0187
0.55	0.010 4	0.007 93	0.001 68-0.0383
0.6	0.021 6	0.017 4	0.003 97-0.0721
0.65	0.040 2	0.035 6	0.011 2-0.113
0.7	0.082 7	0.076	0.024 9-0.239
0.75	0.154	0.148	0.060 0-0.368
0.8	0.289	0.277	0.137-0.560
0.85	0.531	0.509	0.280-0.928
0.9	1.02	0.991	0.587-1.66
0.95	2.25	2.18	1.36-3.49

cases and it needs significant modification for application to 3D problems.

V. CONCLUSION

A new approach for estimating the permeability of a planar porous structure is presented. The approach estimates the pressure drop in various passages of the structure and then calculates the overall pressure drop based on the flow rate distribution. The predictions obtained using this approach are compared with the measured permeability values reported in the literature and the results obtained from other computational approaches. It is shown that the approach can predict the permeability values two orders of magnitude faster than CFD approaches with comparable accuracy. The approach is then used to study the permeability-porosity relationship and its accuracy level at different porosities using 10 000 random structures and the expected permeability range for each porosity is presented.

ACKNOWLEDGMENTS

The first author (S.M.R.N.) acknowledges the Natural Sciences and Engineering Research Council of Canada (NSERC) for a postdoctoral fellowship (PDF).

APPENDIX A: THE STOKES FLOW EQUATION IN THE STREAMLINE COORDINATE SYSTEM

To convert the Stokes flow equation ($\nabla p = \mu \nabla^2 \mathbf{V}$) into the streamline coordinate system (s, n) (with the unit vectors of ($\mathbf{i}_s, \mathbf{i}_n$)), the derivatives of the unit vectors have to be considered

$$\frac{\partial \mathbf{i}_s}{\partial s} = -\frac{\mathbf{i}_n}{\mathcal{R}}, \quad \frac{\partial \mathbf{i}_s}{\partial n} = 0, \quad \frac{\partial \mathbf{i}_n}{\partial s} = \frac{\mathbf{i}_s}{\mathcal{R}}, \quad \frac{\partial \mathbf{i}_n}{\partial n} = 0, \quad (\text{A1})$$

where \mathcal{R} is the streamline's local radius of curvature. The Laplacian operator can then be determined in this coordinate system as

$$\begin{aligned} \nabla^2 &= \nabla \cdot \nabla = \left(\mathbf{i}_s \frac{\partial}{\partial s} + \mathbf{i}_n \frac{\partial}{\partial n} \right) \cdot \left(\mathbf{i}_s \frac{\partial}{\partial s} + \mathbf{i}_n \frac{\partial}{\partial n} \right) \\ &= \frac{\partial^2}{\partial s^2} + \frac{1}{\mathcal{R}} \frac{\partial}{\partial n} + \frac{\partial^2}{\partial n^2}. \end{aligned} \quad (\text{A2})$$

Considering $\mathbf{V} = v_s \mathbf{i}_s$, the Laplacian of the velocity vector can then be obtained as

$$\begin{aligned} \nabla^2 \mathbf{V} &= \left(\frac{\partial^2 v_s}{\partial s^2} + \frac{\partial^2 v_s}{\partial n^2} + \frac{1}{\mathcal{R}} \frac{\partial v_s}{\partial n} - \frac{v_s}{\mathcal{R}^2} \right) \mathbf{i}_s \\ &\quad + \left(\frac{-2}{\mathcal{R}} \frac{\partial v_s}{\partial s} + \frac{v_s}{\mathcal{R}^2} \frac{\partial \mathcal{R}}{\partial s} \right) \mathbf{i}_n. \end{aligned} \quad (\text{A3})$$

Finally, the Stokes flow can be written in the streamline coordinate system as

$$\begin{cases} \frac{\partial p}{\partial s} = \mu \left(\frac{\partial^2 v_s}{\partial s^2} + \frac{\partial^2 v_s}{\partial n^2} + \frac{1}{\mathcal{R}} \frac{\partial v_s}{\partial n} - \frac{v_s}{\mathcal{R}^2} \right), \\ \frac{\partial p}{\partial n} = \mu \left(\frac{-2}{\mathcal{R}} \frac{\partial v_s}{\partial s} + \frac{v_s}{\mathcal{R}^2} \frac{\partial \mathcal{R}}{\partial s} \right). \end{cases} \quad (\text{A4})$$

APPENDIX B: THE DETAILS OF THE SOLUTION ALGORITHM

The porous structure used to explain the various steps used in the solution process is the structure shown in Figure 8 and discussed as a typical example. This domain is composed of a 15×17 mesh structure and it is assumed that the structure is bounded at the left and right by two outer solid boundaries. In other words, it is assumed that the $(0, n)$ and $(16, n)$ cells are the outer surrounding solid boundaries ($1 \leq n \leq 17$). The flow enters from the base and exits at the top. The black cells represent the impervious solid phase. The expected directions of the flow are also indicated by arrows.

1. Passage specification

Figure 8 shows that the flow divides into separate branches and each branch passes through a specific passage of the structure. As an example, the incoming flow first passes through a wide passage and experiences a pressure drop; the flow then divides into three different passages to the left, center, and right (with different pressure drops). The flow in these passages then divides into more branches and some of the new branches subsequently combine. Clearly, as the flow rates in these passages are not determined, the pressure drops cannot be calculated. However, using the discussions presented in the theoretical developments, the pressure drop in each passage can be estimated as a function of the flow rate of that specific passage. To achieve this, these passages have to be specified first.

In Figure 8 different passages are defined for this example; the cells in each passage are specified by identical colors, with a number attached to it. To define the passages, each cell is investigated separately: The first row is inspected and all the adjacent cells that are not separated by a solid cell (boundary cell) are categorized in the same passage. If two groups of cells are separated by solid cells, those are categorized as separate passages. A similar process is used for the third row. The first three adjacent cells are colored khaki and categorized as

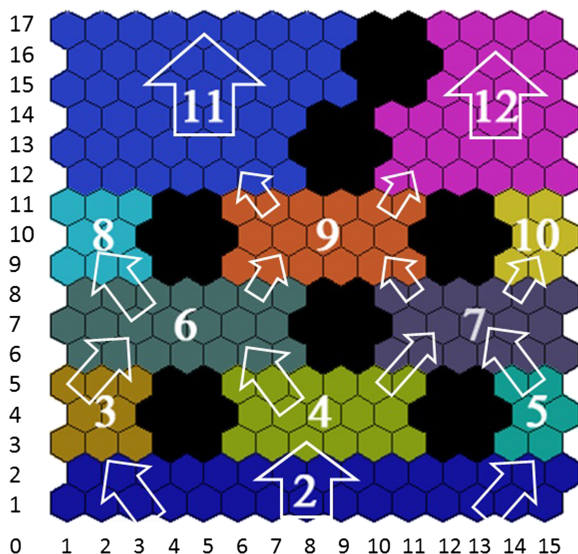


FIG. 8. The porous structure used as the example to explain the algorithm. The arrows demonstrate the expected directions of the flow. The defined passages (2-12) are also shown in different colours.

passage 3. After two solid cells, six adjacent cells are colored yellow green and designated as passage 4. Finally, the last two adjacent cells after two solid cells are categorized as another passage (passage 5). In the first row of Figure 8, however, as there is no solid (black) cell, all the cells are categorized in one passage (passage 2).

When the cells of the first row are categorized, the cells of the subsequent rows are classified in a similar manner. First, the groups of cells in the new row, that are not separated by a black cell, are determined. These cells are identified as being in the same passage as the cells in the row immediately below them, if no other groups are connected to this group in the new row, and the cells in the previous row are not connected to another group of cells in the new row. As an example, the cells of the second row in Figure 8 belong to the same passage as the cells of the first row (passage 2), because there are no other passages in the first row which connect to these cells, and the cells in the first row are not connected to another group of cells in the second row. However, the cells in the third row are categorized into three different passages (3, 4, and 5). While each of them (e.g., passage 3) is only connected to passage 2 in the previous row (second row), the passage 2 itself is connected to the other groups of cells in the third row (i.e., passages 4 and 5). In other words, the flow from passage 2 divides into three parts and therefore just one part of the flow enters passage 3. As a result, passages 2 and 3 have to be separated. It should be noted that the goal of defining the passages is to calculate the pressure drop in each passage as a function of the flow rate in the passage. On the other hand, the first seven cells in the sixth row are defined as a new passage (passage 6); the cells are connected to cells from two different passages in the previous row (i.e., passages 3 and 4). Clearly, all the cells in the left top corner of Figure 8 are categorized in just one passage (passage 11) as the flow is not divided in this region.

When the cells are categorized and the passages are determined, the connections between these passages can be specified. Figure 9 shows the connection tree of the passages defined previously in Figure 8. In this figure, nodes 1 and 13 show the input and output, respectively.

2. Pressure drop estimation

To obtain the pressure drop, the lengths of the surrounding boundaries need to be calculated in each passage. Here, the length of the “left” and “right” boundaries is first obtained. In the calculation process, the “left” boundary is considered to start from the left hand side of the first cell in the first row of the passage. As an example, the left boundary for passage 4 in Figure 8 starts at the cell coordinate of $(5, 3)$. Similarly, the left boundary of the passage 8 starts from the cell $(0, 9)$. The left boundary follows the passage and rotates clockwise around the passage to reach the next passage (or output). As an example, the left boundary for the passages 3 and 12 contain the cells $[(0, 3), (0, 4), (0, 5), (0, 6)]$ and $[(9, 12), (10, 13), (9, 14), (10, 15), (11, 15), (11, 16), (11, 17)]$, respectively.

A similar algorithm is used to determine the “right” boundary. The right boundary begins at the right hand side of the last cell in the first row of the passage. As an example, for passage 4 the right boundary starts from the cell $(12, 3)$

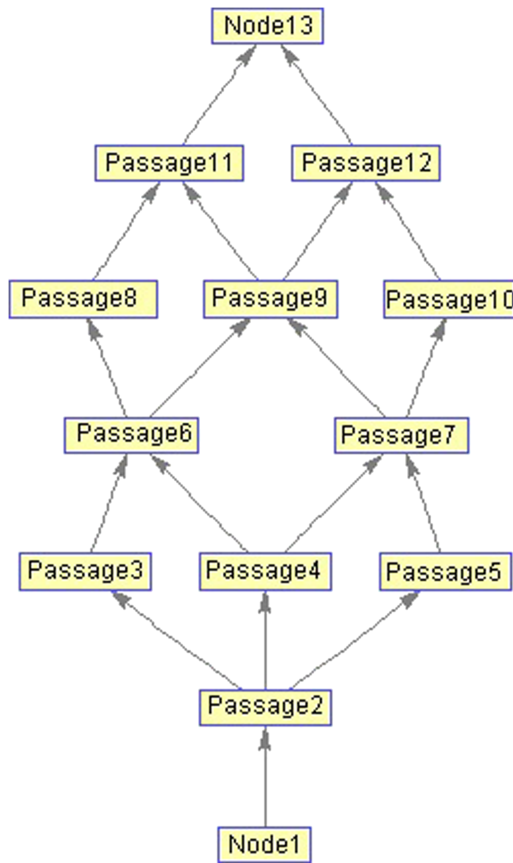


FIG. 9. The connection tree between the passages.

and at (4,9) for passage 8. Here, the right boundary rotates counter-clockwise around the passage to reach the next passage (or output). As a result, the right boundary for passages 8 and 10 contains the cells [(4,9), (3,10), (4,11)] and [(16,9), (16,10), (16,11)], respectively.

When the cells of the left and right boundaries are determined, the width of the passage for each cell on the boundary can be calculated. For each cell on the left and right boundaries, the width is defined as the distance between that cell and the closest cell on the opposite boundary. As an example, for cell (11,16) on the left boundary of the passage 12, the neighbour cells inside the passage (e.g., [(12,15), (12,16), (12,17)]) are obtained. Then, the next layer of the cells beside this layer and inside the passage is found (i.e., [(12,14), (13,15), (13,16), (13,17)]). As these cells do not belong to the opposite boundary (right boundary), the next layer is investigated (i.e., [(13,13), (13,14), (14,15), (14,16), (14,17)]). The process continues to the next layer, and finally the cell (16,16) is found and the passage width for the cell (i.e., cell (11,16)) is determined.

Two points should be emphasized: First, as the algorithm continues to find a boundary cell on the “opposite boundary,” local cavities will not lead to computational errors. As an example, when the algorithm is calculating the width for the cell (10,13) on the left boundary of passage 12, it does not consider the cell (11,15) as the boundary, as it is not on the “opposite” (here, right) boundary. Clearly, if the cell (11,15) is considered as the boundary, then the calculated width would be incorrect. Second, as the algorithm looks

for the opposite boundary radially, it also works when the flow direction is not vertical. In other words, if the “left” and “right” boundaries sit above and below a passage, as the algorithm finds the closest cell on the opposite boundary using a radial investigation, it can estimate the pressure drop with the same accuracy. This point is also examined and discussed in Figure 5(d).

When the width estimation for the cells on both boundaries is completed, the pressure drop is calculated for each boundary separately using the length of the boundary and the width of the passage at each point. These two pressure drops are then averaged and the pressure drop for the passage is determined as a function of the flow rate.

3. Structure correction

In this step, the dead-end passages are removed from the network. A dead-end passage is defined as a passage or a set of passages that have just one connection to the network. These passages are assumed to have a negligible effect on the overall pressure drop of the structure and are therefore not considered in the calculation process. It is important to locate and remove these dead-end passages since they could introduce errors in the initial estimate for the flow rates, which cannot be corrected in subsequent steps. In the example discussed here (Figure 8), no such corrections are required and as a result, the network shown in Figure 9 is considered to be the final network and is used in Appendixes B 4–B 6.

4. Connection loss estimation

As mentioned, the connection loss is approximated using the initial estimate for the flow rate distribution, which is determined as follows: for each passage, the input flow rates are determined and summed and this flow rate is distributed between the output passages based on the ratio of their pressure drops. Using this method, the mass conservation is satisfied for the initial flow rate assumption (which is crucial for the Hardy Cross method). Moreover, this estimation results in an accurate flow rate distribution, if the output passages are connected together in the next level. Clearly, this initial estimate is not always correct and should be modified by considering the overall structure. This problem is solved in Appendixes B 5 and B 6.

5. Finding the loops

In order to employ the Hardy Cross method to calculate the flow rate distribution in the structure (i.e., the connection tree shown in Figure 9), it is necessary to detect all the loops in the structure. The goal of the loop detection process is to correct the flow rates on the loops such that the pressure drop in parallel passages becomes equal. Therefore, as an example, passages 2-3-6-4-2 and 2-3-6-9-7-4-2 in Figure 9 make two separate loops, which cannot be considered as “independent” loops for passage 2 since passage 5 is not considered in this process. Hence, the loop detection process for a passage (e.g., passage 2 in Figure 9) can be terminated if all the output passages (here, passages 3, 4, and 5) appear in the resultant loops. Considering this point, the loops are detected as follows: For each passage that has more than

one output (passages 2, 4, 6, 7, and 9 in Figure 9), the output passages are recorded. A loop is considered “detected” if it contains at least one new output passage of the first level. As a result, the loops discussed above (e.g., 2-3-6-4-2 and 2-3-6-9-7-4-2) are identical (because they both pass from the same first level outputs 3 and 4) and therefore, just one of them is recorded.

This process can be explained by the following example. To find the loops starting from passage 2, the output passages (i.e., passages 3, 4, and 5) are recorded. In the next level, passage 6 is recorded as the output of passage 3. When the outputs of passage 4 are investigated, it is found that passage 6 was recorded before, and, as a result, a loop 2-3-6-4-2 is detected. Similarly, the loop 2-4-7-5-2 is detected. As the detected loops include all the outputs of the passage 2 (i.e., passages 3, 4, and 5), the loop detection process for passage 2 is terminated and the algorithm continues to investigate the next passages.

6. Modification of the Hardy Cross method

The Hardy Cross method is a self-correcting iterative method to determine the flow rate distribution in a pipe network.³⁴ In this method, the flow rate in each loop is corrected such that the pressure drop in parallel pipes in the loop becomes equal. This method is used here to solve the network in the porous structure (e.g., network shown in Figure 9 for the example discussed here). However, the Hardy Cross method cannot be used directly for this problem and needs to be modified. In a pipe network, the pressure drop occurs in the connecting pipes while here the pressure drop occurs in the nodes (passages) themselves (the connection losses are also added to the passages).

This can be explained through the following example. The loop 2-3-6-4-2 in Figure 9 is considered. The flow enters this loop from passage 2 and exits through passage 6. As a result, the equal-pressure-drop-in-parallel-passage condition is achieved if the flow rate is distributed such that the pressure drop in passages 3 and 4 is equal. In other words, the pressure drops of passages 2 and 6 are not considered in the calculation process. As a result, the Hardy Cross method needs to be modified for this specific application as follows:

1. For each loop, the input and output passages are identified. The input passage is the passage that does not have any input from the passages within the loop. Similarly, the output passage in the loop is the passage that has no output to other passages in the loop.
2. The passages between the input and output passages in different paths are specified.
3. Similar to the Hardy Cross method, the pressure drops are algebraically summed considering the flow direction.
4. The flow rate in the loop is corrected.
5. If the flow rate in a passage is evaluated as negative, the network is corrected and the input and output passages are re-determined; the process is then repeated from the first step.
6. The process continues for all the loops until the flow rates in all the loops are converged.

When the flow rate distribution is determined, the overall pressure drop of the structure can be calculated using any passage that connects the input (node 1) to the output (here, node 13). Clearly, the calculated pressure drop would be independent of the passage. Since the flow pressure drop in all the paths connecting the input to the output is equal, it can be stated that the flow rate distribution is calculated such that the fluid energy dissipation in the structure is independent of the fluid path and as a result, the flow is stabilized.

- ¹K. Yazdchi, S. Srivastava, and S. Luding, “Microstructural effects on the permeability of periodic fibrous porous media,” *Int. J. Multiphase Flow* **37**, 956 (2011).
- ²J. T. Gostick, M. W. Fowler, M. D. Pritzker, M. A. Ioannidis, and L. M. Behra, “In-plane and through-plane gas permeability of carbon fiber electrode backing layers,” *J. Power Sources* **162**, 228 (2006).
- ³J. A. Weibel, S. V. Garimella, and M. T. North, “Characterization of evaporation and boiling from sintered powder wicks fed by capillary action,” *Int. J. Heat Mass Transfer* **53**, 4204 (2010).
- ⁴A. E. Scheidegger, *The Physics of Flow through Porous Media* (University of Toronto Press, Toronto, 1974).
- ⁵A. Gueven, and Z. Hicsasmaz, *Pore Structure in Food: Simulation, Measurement and Applications* (Springer, New York, 2013).
- ⁶J. Bear, *Dynamics of Fluids in Porous Media* (Dover Publications, New York, 1972).
- ⁷J. Bear, and A. H.-D. Cheng, *Modeling Groundwater Flow and Contaminant Transport* (Springer, New York, 2010).
- ⁸B. Ghanbarian, A. G. Hunt, R. P. Ewing, and M. Sahimi, “Tortuosity in porous media: A critical review,” *Soil Sci. Soc. Am. J.* **77**, 1461 (2013).
- ⁹Y. Matsumura and T. L. Jackson, “Numerical simulation of fluid flow through random packs of polydisperse cylinders,” *Phys. Fluids* **26**, 123302 (2014).
- ¹⁰Y. Matsumura and T. L. Jackson, “Numerical simulation of fluid flow through random packs of cylinders using immersed boundary method,” *Phys. Fluids* **26**, 043602 (2014).
- ¹¹Y. Matsumura, D. Jenne, and T. L. Jackson, “Numerical simulation of fluid flow through random packs of ellipses,” *Phys. Fluids* **27**, 023301 (2015).
- ¹²D. Maggiolo, F. Picano, and M. Guarnieri, “Flow and dispersion in anisotropic porous media: A lattice Boltzmann study,” *Phys. Fluids* **28**, 102001 (2016).
- ¹³V. Joekar-Niasar and S. M. Hassanizadeh, “Analysis of fundamentals of two-phase flow in porous media using dynamic pore-network models: A review,” *Crit. Rev. Environ. Sci. Technol.* **42**, 1895 (2012).
- ¹⁴C. Louriou and M. Prat, “Pore network study of bubble growth by vaporisation in a porous medium heated laterally,” *Int. J. Therm. Sci.* **52**, 8 (2012).
- ¹⁵M. Blunt, M. D. Jackson, M. Piri, and P. H. Valvatne, “Detailed physics, predictive capabilities and macroscopic consequences for pore-network models of multiphase flow,” *Adv. Water Res.* **25**, 1069 (2002).
- ¹⁶R. J. Held and M. A. Celia, “Modeling support of functional relationships between capillary pressure, saturation, interfacial area and common lines,” *Adv. Water Res.* **24**, 325 (2001).
- ¹⁷A. P. S. Selvadurai, *Partial Differential Equations in Mechanics, The Biharmonic Equation, Poisson’s Equation Vol. 2* (Springer-Verlag, Berlin, 2000).
- ¹⁸S. Zobel, B. Maze, H. V. Tafreshi, Q. Wang, and B. Pourdeyhimi, “Simulating permeability of 3-D calendered fibrous structures,” *Chem. Eng. Sci.* **62**, 6285 (2007).
- ¹⁹O. P. Bergelin, G. A. Brown, H. L. Hull, and F. W. Sullivan, “Heat transfer and fluid friction during viscous flow across banks of tubes: III—a study of tube spacing and tube size,” *Trans. ASME* **72**, 881 (1950).
- ²⁰A. A. Kirsch and N. A. Fuchs, “Studies on fibrous aerosol filters -II. Pressure drops in systems of parallel cylinders,” *Ann. Occup. Hyg.* **10**, 23 (1967).
- ²¹T. A. K. Sadiq, S. G. Advani, and R. S. Parnas, “Experimental investigation of transverse flow through aligned cylinders,” *Int. J. Multiphase Flow* **21**, 755 (1995).
- ²²B. Khomami and L. D. Moreno, “Stability of viscoelastic flow around periodic arrays of cylinders,” *Rheol. Acta* **36**, 367 (1997).
- ²³W. H. Zhong, I. G. Currie, and D. F. James, “Creeping flow through a model fibrous porous medium,” *Exp. Fluids* **40**, 119 (2006).

- ²⁴A. Tamayol and M. Bahrami, "Transverse permeability of fibrous porous media," *Phys. Rev. E* **83**, 046314 (2011).
- ²⁵A. Tamayol and M. Bahrami, "Analytical determination of viscous permeability of fibrous porous media," *Int. J. Heat Mass Transfer* **52**, 2407 (2009).
- ²⁶J. Happel, "Viscous flow relative to array of cylinders," *AIChE J.* **5**, 174 (1959).
- ²⁷J. V. Westhuizen and J. P. Du Plessis, "An attempt to quantify fibre bed permeability utilizing the phase average Navier-Stokes equation," *Composites, Part A* **27**, 263 (1996).
- ²⁸E. J. Wiggins, W. B. Campbell, and O. Maass, "Determination of the specific surface of fibrous materials," *Can. J. Res.* **17**, 318 (1939).
- ²⁹P. C. Carman, "The determination of the specific surface of powders. I," *Soc. Chem. Ind. (Trans. Commun.)* **57**, 225 (1938).
- ³⁰A. G. Kostornov and M. S. Shevchuk, "Hydraulic characteristics and structure of porous metal fibre materials," *Powder Metall. Met. Ceram.* **16**, 694 (1977).
- ³¹C. N. Davies, *The Separation of Airborne Dust and Particles* (Institute of Mechanical Engineers, London, 1952), Vol. B1, p.185.
- ³²M. A. Van Doormaal and J. G. Pharoah, "Determination of permeability in fibrous porous media using the lattice Boltzmann method with application to PEM fuel cells," *Int. J. Numer. Methods Fluids* **59**, 75 (2009).
- ³³M. M. Tomadakis and T. Robertson, "Viscous permeability of random fiber structures: Comparison of electrical and diffusional estimates with experimental and analytical results," *J. Compos. Mater.* **39**, 163 (2005).
- ³⁴H. Cross, *Analysis of Flow in Networks of Conduits or Conductors* (University Illinois Bulletin, 1936), Vol. 282.